Electronic structure of the high-T_C ferromagnetic semiconductor (Ga,Fe)Sb: X-ray magnetic circular dichroism and resonance photoemission spectroscopy studies

Shoya Sakamoto,[1] Nguyen Thanh Tu,[2] Yukiharu Takeda,[3] Shin-ichi Fujimori,[3] Pham Nam Hai,[4,5] Le Duc Anh,[2,6]
Yuki K. Wakabayashi,[2] Goro Shibata,[1] Masafumi Horio,[1] Keisuke Ikeda,[1] Yuji Saitoh,[3] Hiroshi Yamagami,[3,7]
Masaaki Tanaka,[2,5] and Atsushi Fujimori[1]
[1]*Department of Physics, The University of Tokyo, Bunkyo-ku, Tokyo 113-0033, Japan*
[2]*Department of Electrical Engineering and Information Systems, The University of Tokyo, Bunkyo-ku, Tokyo 113-8656, Japan*
[3]*Materials Sciences Research Center, Japan Atomic Energy Agency, Sayo-gun, Hyogo 679-5148, Japan*
[4]*Department of Electrical and Electronic Engineering, Tokyo Institute of Technology, Meguro-ku, Tokyo 152-0033, Japan*
[5]*Center for Spintronics Research Network, The University of Tokyo, Bunkyo-ku, Tokyo 113-8656, Japan*
[6]*Institute of Engineering Innovation, The University of Tokyo, Bunkyo-ku, Tokyo 113-8656, Japan*
[7]*Department of Physics, Kyoto Sangyo University, Kyoto 603-8555, Japan*

(Received 20 November 2018; revised manuscript received 11 May 2019; published 15 July 2019)

The electronic structure and the magnetism of the ferromagnetic semiconductor (Ga,Fe)Sb, whose Curie temperature T_C can exceed room temperature, were investigated by means of x-ray absorption spectroscopy (XAS), x-ray magnetic circular dichroism (XMCD), and resonance photoemission spectroscopy (RPES). The line-shape analyses of the XAS and XMCD spectra suggest that the ferromagnetism is of intrinsic origin. The orbital magnetic moments deduced using XMCD sum rules were found to be large, indicating that there is a considerable $3d^6$ contribution to the ground state of Fe. From RPES, we observed a strong dispersive Auger peak and nondispersive resonantly enhanced peaks in the valence-band spectra. The latter is a fingerprint of the correlated nature of Fe $3d$ electrons, whereas the former indicates their itinerant nature. It was also found that the Fe $3d$ states have a finite contribution to the density of states at the Fermi energy. These states, presumably consisting of majority-spin p-d hybridized states or minority-spin e states, would be responsible for the ferromagnetic order in this material.

DOI: 10.1103/PhysRevB.100.035204

I. INTRODUCTION

Creating functional devices exploiting the spin degree of freedom in semiconductors has been one of the major challenges in the field of electronics [1–3]. Under such circumstances, magnetically doped semiconductors, or diluted magnetic semiconductors, have attracted much attention since they possess both magnetic and semiconducting properties [4–9]. Mn-doped III-V semiconductors such as (In,Mn)As [10,11] and (Ga,Mn)As [12–14] have been extensively studied because they exhibit carrier-induced ferromagnetism, where the ferromagnetic interaction between the Mn magnetic moments is mediated by hole carriers, and it is possible to control the ferromagnetism through changing the carrier concentration by gate voltage [15,16] or light irradiation [17].

Despite those attractive features, they also have shortcomings for practical applications: their Curie temperatures T_C are much lower than room temperature, 90 K for (In,Mn)As [18] and 200 K for (Ga,Mn)As [19]; only p-type conductivity is realized since Mn always acts as an acceptor at the substitutional In^{3+} or Ga^{3+} sites.

Recently, Fe-doped ferromagnetic III-V semiconductors (In,Fe)As:Be [20–22], (Ga,Fe)Sb [23–25], (Al,Fe)Sb [26], and (In,Fe)Sb [27–29] were synthesized and exhibit some advantages over the Mn-doped ones. If Fe substitutes for the In^{3+} or Ga^{3+} site and takes the stable valence of 3+ with the $3d^5(4sp)^3$ configuration, no charge carrier will be provided, and hence, both n- and p-type conduction will be possible via additional carrier doping. In fact, (Al,Fe)Sb is insulating; (In,Fe)As:Be is n type, where doped interstitial Be atoms act as double donors, and (Ga,Fe)Sb is p type, where native charged defects such as Ga antisites are thought to act as acceptors and provide holes. The T_C's of these materials are relatively high and increase as the Fe content increases, reaching 70 K for (In,Fe)As:Be with 8% Fe doping [22], 40 K for (Al,Fe)Sb with 10% Fe [26], 335 K for (In,Fe)Sb [27] with 16% Fe, and 340 K for (Ga,Fe)Sb [25] with 25% Fe. It has been found that the distribution of Fe atoms is nonuniform in the zinc-blende crystal structure of these materials, which seems to play an important role in stabilizing the ferromagnetic order [24,26,30]. However, the microscopic origin of the ferromagnetism in terms of their electronic structures has not been clarified yet and remains to be investigated. For this purpose, we have performed soft x-ray absorption spectroscopy (XAS), x-ray magnetic circular dichroism (XMCD), and resonance photoemission spectroscopy (RPES) studies of (Ga,Fe)Sb.

XAS and XMCD at the $L_{2,3}$ absorption edges of the $3d$ transition metals are very powerful methods for the purpose of clarifying the electronic structures related to the ferromagnetism. Since x-ray absorption takes place at a specific constituent atom, one can obtain element-specific information about the electronic structure and its relation to the magnetism, excluding extrinsic effects such as the diamagnetic

2469-9950/2019/100(3)/035204(8)

©2019 American Physical Society

contribution from the substrate. XMCD sum rules make it possible to obtain the spin and orbital magnetic moments of the constituent atoms separately [31,32]. In addition to XAS and XMCD, RPES has frequently been employed as a direct probe to examine the electronic structure of materials. RPES provides the information about the partial density of states (PDOS) of a $3d$ transition-metal element and has been used to study the electronic structures of ferromagnetic semiconductors (FMSs) such as (Ga,Mn)As [33,34], Ge:Fe [35], and (Ba,K)(Zn,Mn)$_2$As$_2$ [36,37]. Moreover, the combination of RPES and XMCD yields the PDOS of only ferromagnetically active components and is suitable for studying FMSs, where doped magnetic atoms are often oxidized at the surface.

II. EXPERIMENT

Ga$_{1-x}$Fe$_x$Sb films with two different Fe contents, $x = 6.0\%$ and 13.7% (referred to as samples A and B, respectively), were grown on GaAs(001) substrates using the low-temperature molecular beam epitaxy method. To relax the lattice mismatch between (Ga,Fe)Sb and GaAs, three buffer layers were inserted; initially, GaAs (50 nm) and AlAs (10 nm) layers were successively grown at a substrate temperature T_S of 550 °C, and then an AlSb (100 nm) layer was grown at $T_S = 470\,^\circ$C. After growing the buffer layers, a 50-nm-thick (Ga,Fe)Sb layer was grown. Here, T_S was set to 200 °C for sample A and 250 °C for sample B. Last, a subnanometer-thick amorphous As cap layer was deposited to prevent surface oxidation. Note that sample A was paramagnetic down to 5 K, and sample B was ferromagnetic with $T_C = 170$ K. In order to remove the oxidized surface, we etched the sample with hydrochloric acid (HCl; 2.4 mol/L) for 5 s and subsequently rinsed it with water just before loading the sample in the vacuum chamber of the spectrometer [35,38].

All the measurements were performed at beamline BL23SU of SPring-8. Circularly polarized x rays of 690–780 eV were used for both absorption and photoemission measurements. For XMCD measurements, a magnetic field was applied parallel to the incident x rays and perpendicular to the sample surface. Absorption signals were taken in the total electron yield mode, and dichroic signals were measured by reversing the helicity of the x rays with 1-Hz frequency at each photon energy under a fixed magnetic field. In order to eliminate spurious XMCD signals, the scans were repeated with opposite magnetic field directions. Each XMCD spectrum was obtained as the average, namely, $(\sigma_{+,h} - \sigma_{-,h}) + (\sigma_{-,-h} - \sigma_{+,-h})$, where σ denotes the absorption cross sections, the first subscript indicates the helicity of the x rays, and the second subscript gives the sign of the magnetic field. XAS was obtained as the summation of all four terms. Note that a two-step inverse tangent function representing the Fe $L_{2,3}$-edge jumps was subtracted from each term [39].

For RPES measurements, the sample temperature was set to 100 K, and the energy resolution was about 150 meV. The samples were placed so that the [−110] direction became parallel to the analyzer slit and perpendicular to the beam. Photoelectrons were collected in the normal emission geometry with 45° light incidence.

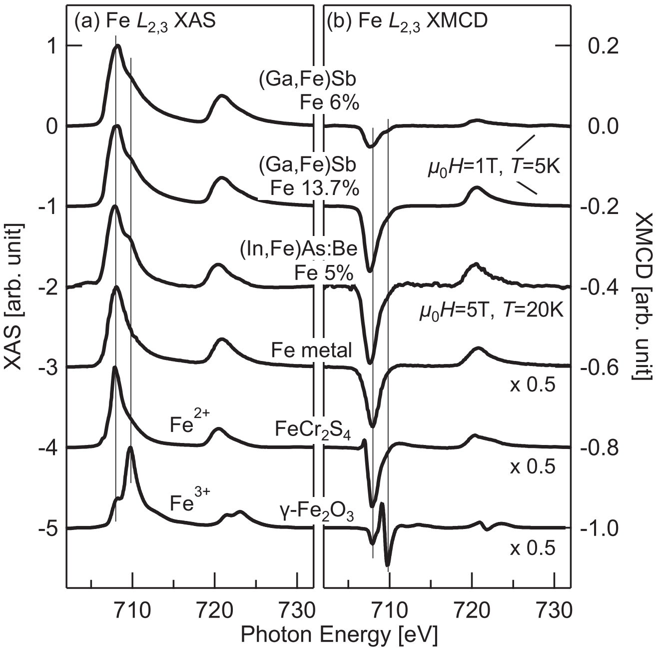

FIG. 1. (a) XAS and (b) XMCD spectra of (Ga,Fe)Sb compared with those of (In,Fe)As:Be [30], bcc Fe [37,39], FeCr$_2$O$_4$ [40], and γ-Fe$_2$O$_3$ [41]. The XMCD spectra of bcc Fe, FeCr$_2$O$_4$, and γ-Fe$_2$O$_3$ are multiplied by 0.5 for ease of comparison.

III. RESULTS AND DISCUSSION

A. XAS and XMCD

Figures 1(a) and 1(b) show XAS and XMCD spectra of the present (Ga,Fe)Sb films after the HCl etching compared with those of (In,Fe)As:Be [30], Fe metal [39], FeCr$_2$S$_4$ [40], and γ-Fe$_2$O$_3$ [41]. Note that the Fe $3d$ electrons in FeCr$_2$S$_4$ and γ-Fe$_2$O$_3$ are localized and that the valence of Fe is 2+ in FeCr$_2$S$_4$ and 3+ in γ-Fe$_2$O$_3$.

The line shapes of the spectra of the two (Ga,Fe)Sb films resemble those of bcc Fe metal rather than the sharper spectra of FeCr$_2$S$_4$, manifesting the itinerant nature of the Fe $3d$ electrons in (Ga,Fe)Sb. Although the spectral line shapes of the two (Ga,Fe)Sb films look almost identical, representing nearly the same electronic structure, the intensity of the XMCD signals was significantly suppressed for the 6% Fe-doped sample compared with the 13.7% Fe-doped sample simply because only the 13.7% Fe-doped sample exhibits ferromagnetism while the 6% Fe-doped one is paramagnetic at 5 K. Such an insensitivity of the line shape to transition-metal content was also reported for (Ga,Mn)As [42], (In,Fe)As:Be [30], etc.

In addition to the main peak at ∼708 eV, there is a shoulder at ∼710 eV, which is more evident in XAS than in XMCD. This can be attributed to Fe^{3+} oxides forming at the surface because the feature at ∼710 eV was prominent before etching and disappeared almost completely after etching, as shown in Fig. 2. Here, the spectra of both paramagnetic and ferromagnetic samples after etching resemble those of Ge:Fe and (In,Fe)As:Be. Using these two spectra containing different degrees of contribution from surface oxides, it was possible to deduce the intrinsic spectra as $[\mathrm{XAS}]_{\mathrm{int}} \propto [\mathrm{XAS}]_{\mathrm{a}} - p[\mathrm{XAS}]_{\mathrm{b}}$. Here, $[\mathrm{XAS}]_{\mathrm{a}}$ and $[\mathrm{XAS}]_{\mathrm{b}}$ denote the XAS spectrum after and before etching, respectively, and p

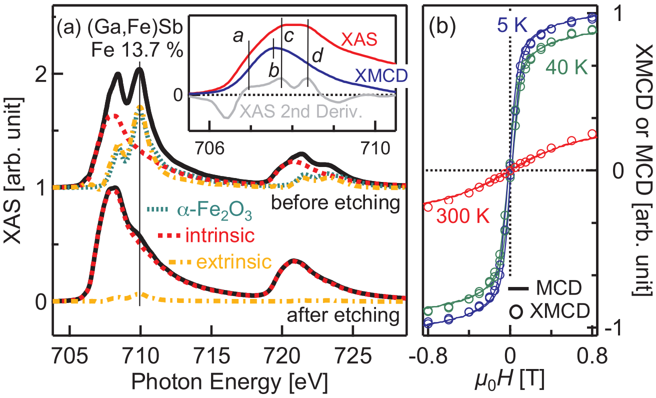

FIG. 2. (a) XAS and XMCD spectra of the 13.7% Fe-doped (Ga,Fe)Sb before and after HCl etching. Intrinsic and extrinsic components are also separately shown by red and orange dashed curves, respectively, together with the spectrum of α-Fe_2O_3. The inset shows the intrinsic XAS and XMCD spectra expanded at the Fe L_3 edge. The second derivative of the XAS spectrum is also shown to emphasize weak features, labeled *a*–*d*. Here, the signs of the XMCD and the second derivative spectrum have been reversed. (b) Magnetic-field dependence of XMCD and visible-light MCD intensities, shown by circles and solid curves, respectively.

was chosen so that the shoulder at ~710 eV vanished or the second derivative of $[\mathrm{XAS}]_{\mathrm{int}}$ did not show a peak at ~710 eV, as shown in the inset of Fig. 2. The extrinsic contribution from the surface oxides to the XAS spectra was also extractable in a similar manner as $[\mathrm{XAS}]_{\mathrm{ext}} \propto [\mathrm{XAS}]_{\mathrm{a}} - q[\mathrm{XAS}]_{\mathrm{b}}$, where q was chosen so that $[\mathrm{XAS}]_{\mathrm{ext}}$ became identical to the spectra of α-Fe_2O_3 shown by the green dashed curve. Thus-obtained intrinsic and extrinsic components are separately shown in Fig. 2 by red and orange dashed curves, respectively, for both spectra before and after etching. From this procedure, it was found that the extrinsic contribution to the XAS was almost ~60 % before etching and was significantly reduced to ~4% after etching, which guarantees the efficiency of HCl etching.

In order to see subtle features in the spectra, the "intrinsic XAS" and XMCD spectra at the Fe L_3 edge are shown in the inset of Fig. 2 together with the second derivative of the XAS spectrum to highlight weak shoulders in the XAS spectrum labeled *a*–*d*. Here, the signs of XMCD and the second-derivative XAS spectra are reversed for ease of comparison. The XAS spectrum of (Ga,Fe)Sb mainly consists of two features, *c* and *d*, which do not exactly coincide with the feature in XMCD (labeled *b*). This is not the case for bcc Fe, where the XAS spectrum consists of a broad single peak, and the peak positions of XAS and XMCD indeed coincide [30]. Such a peak-position difference may indicate the presence of multiple phases containing Fe atoms, most likely due to the Fe density fluctuation forming Fe-poor and Fe-rich regions. Such behavior was also found in (In,Fe)As:Be and Ge:Fe and may be a universal feature of Fe-doped semiconductors. Note that there is also a shoulder at ~710 eV in the XMCD spectra originating from Fe^{3+} oxides, but the contribution is much smaller.

In Fig. 2(b), we compare the magnetic-field dependence of the XMCD intensity (XMCD-*H* curve) at the Fe L_3 edge and that of visible-light magnetic circular dichroism (MCD) intensities (MCD-*H* curve) measured at the E_1 absorption edge of GaSb. The XMCD and MCD data are shown by open circles and solid curves, respectively. Note that the XMCD-*H* curves were measured after the etching, while the MCD-*H* curves were measured before the etching. The fact that the surface-sensitive XMCD-*H* curves agree well with the relatively bulk sensitive MCD-*H* curves guarantees that the signals observed in this study are intrinsic.

TABLE I. Spin and orbital magnetic moments of Fe in (Ga,Fe)Sb in comparison with those of (In,Fe)As:Be, Ge:Fe, and bcc Fe metal. All the values have been estimated using the XMCD sum rules [Eqs. (1) and (2)], except for the ones in the third and fourth rows, which were computed using the GGA and GGA+U methods.

	$m_{\mathrm{orb}}/m_{\mathrm{spin}}$	m_{orb}	m_{spin}
$Ga_{0.94}Fe_{0.06}Sb$[a]	0.13 ± 0.01	0.05[b]	0.37[b]
$Ga_{0.863}Fe_{0.137}Sb$[a]	0.13 ± 0.01	0.14[b]	1.07[b]
$In_{0.9}Fe_{0.1}As$:Be[a] [30]	0.10 ± 0.02	0.17[c]	1.75[c]
$Ge_{0.935}Fe_{0.065}$[a] [47]	0.11 ± 0.03	0.14[b]	1.29[b]
Fe bcc [39]	0.043 ± 0.001	0.085	1.98

[a] Fe^{2+} configurations were assumed.

[b] Values at $\mu_0 H = 1$ T and $T = 5$ K.

[c] Values at 5 T and 20 K.

By applying the XMCD sum rules, we have estimated the spin and orbital magnetic moments of Fe [31,32] as follows:

$$m_{\mathrm{orb}} = -\frac{4\int_{L_{2,3}} \mathrm{XMCD}\, d\omega}{3\int_{L_{2,3}} \mathrm{XAS}\, d\omega} n_h, \tag{1}$$

$$m_{\mathrm{spin}} = -\frac{6\int_{L_3} \mathrm{XMCD}\, d\omega - 4\int_{L_{2,3}} \mathrm{XMCD}\, d\omega}{\int_{L_{2,3}} \mathrm{XAS}\, d\omega} n_h, \tag{2}$$

where m_{orb} and m_{spin} are the orbital and spin magnetic moments in units of μ_{B}, respectively, and n_h is the number of 3*d* holes. Here, we have ignored the magnetic dipole term, which is negligibly small for an atomic site with high symmetry such as T_d or O_h [43], and n_h was set to 4, assuming the valence of Fe is 2+ with six 3*d* electrons, as implied by the density functional theory calculation [44]. The correction factor of 0.875 for the Fe^{2+} ion [45,46] was used to estimate the spin magnetic moment. Note that if we assume the Fe^{3+} state with five 3*d* electrons and the correction factor to be 0.685, the spin and orbital magnetic moments would be changed by a factor of 1.6 [= (0.875/0.685) × (5/4)]. The raw XAS and XMCD spectra after etching are used for the sake of simplicity because the extrinsic contribution was only a few percent.

Table I summarizes the spin and orbital magnetic moments of various Fe compounds, including other Fe-doped semiconductors and bcc Fe. It was found that the $m_{\mathrm{orb}}/m_{\mathrm{spin}}$ ratio of (Ga,Fe)Sb is substantially larger than that of bcc Fe. This may be due to the stronger localization of Fe 3*d* electrons [48] in bulk (Ga,Fe)Sb or at the interface between the Fe-rich and Fe-poor regions, where the translational symmetry is broken [49]. The large value of $m_{\mathrm{orb}}/m_{\mathrm{spin}}$ suggests that a considerable fraction of Fe atoms has a valence of 2+ with six 3*d* electrons because the orbital magnetic moments would be quenched if all the Fe atoms took the high-spin Fe^{3+} ($3d^5$) configuration. Nevertheless, there probably exist a significant number of Fe^{3+} ions as

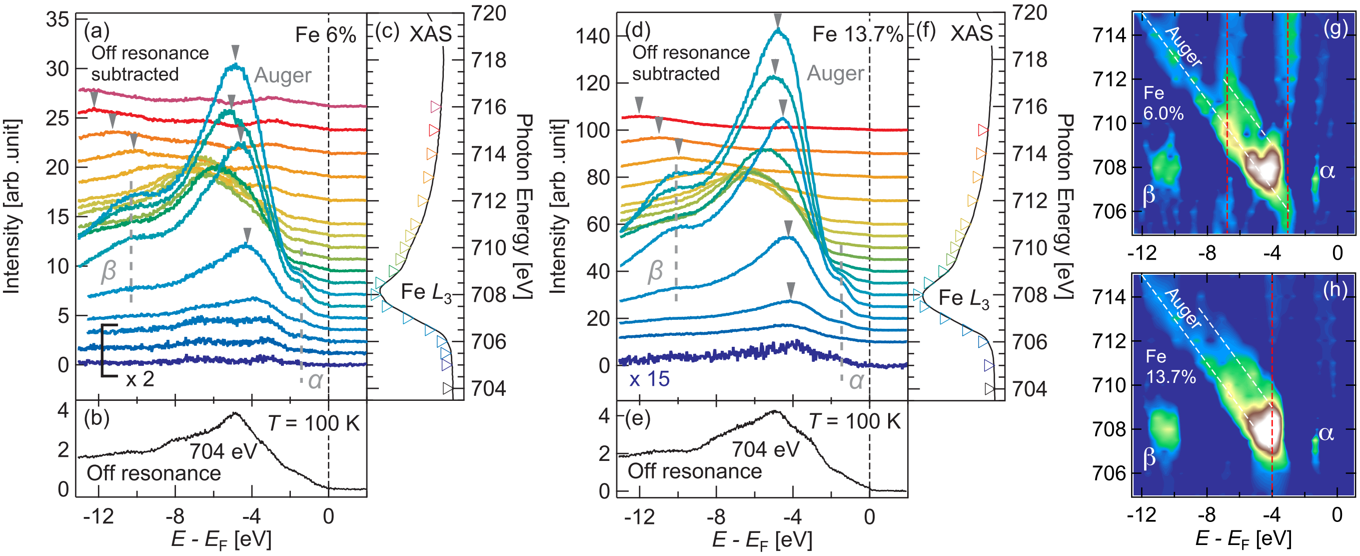

FIG. 3. (a) and (d) Resonance photoemission spectroscopy (RPES) spectra of (Ga,Fe)Sb with 6% Fe and 13.7% Fe taken with photon energies across the Fe L_3 absorption edge. The color and the baseline positions of the spectra represent the photon energies as depicted by triangles on the XAS spectra in (c) and (f). Here, the off-resonance spectra shown in (b) and (e) have been subtracted from all the spectra. (g) and (h) False-color plots of the second derivatives of the RPES spectra in (a) and (d). The dispersive normal Auger peak and the nondispersive resonance features are indicated by white dashed lines and red dashed lines, respectively.

well considering the inhomogeneous nature of the material. Such a large orbital magnetic moment was also observed for (In,Fe)As:Be [30] and Ge:Fe [47]. This fact and the similar spectral line shapes among the above-mentioned Fe-doped FMSs imply that the local electronic structure of Fe is similar and the ferromagnetism has a common origin. Note that the $m_{\mathrm{orb}}/m_{\mathrm{spin}}$ ratio is more unambiguous than the absolute values of m_{orb} and m_{spin} since it contains neither the uncertainty in estimating n_h nor extrinsic contributions to the XAS area.

The deduced spin magnetic moments at $H = 1$ T and $T = 5$ K for both the paramagnetic and ferromagnetic samples are small ($0.37\mu_{\mathrm{B}}$/Fe and $1.07\mu_{\mathrm{B}}$/Fe, respectively) compared with the ionic value of $4\mu_{\mathrm{B}}$ [50] and the experimental saturated magnetic moment of $2.4\mu_{\mathrm{B}}$–$2.9\mu_{\mathrm{B}}$ measured at the same temperature of 5 K [24]. Although the cause of the small deduced magnetic moment is unclear at the present stage, it may be attributed to the existence of nonmagnetic or antiferromagnetic Fe-related impurities near the surface because the XMCD-*H* curves and MCD-*H* curves showed excellent agreement with each other, as shown in Fig. 2(b), indicating that there are almost no extrinsic magnetic components.

B. Resonance photoemission

Figures 3(a) and 3(d) show RPES spectra of the 6% and 13.7% Fe-doped samples, respectively, taken across the Fe L_3 absorption edge from 705 to 716 eV. The color and the baseline positions represent the photon energies indicated by triangles on the XAS spectra in Figs. 3(c) and 3(f). Here, off-resonance spectra taken with a photon energy of 704 eV shown in Figs. 3(b) and 3(e) have been subtracted to emphasize the resonance behavior. Note that the units of the vertical axes of Figs. 3(a), 3(b), 3(d), and 3(e) are the same. For both samples with different Fe contents, a strong normal Auger peak dispersing with incident photon energy was observed. This suggests that the Fe 3*d* electrons in (Ga,Fe)Sb have itinerant character, as already suggested by the XAS measurements, since Auger decay is a consequence of faster screening of the core hole than the recombination of the excited electron with the core hole and is normally observed in metallic systems [51,52]. The observed itinerant character, despite the low carrier concentration of (Ga,Fe)Sb, suggests that there exists a spatial Fe-concentration fluctuation which leads to the formation of Fe-rich locally metallic regions. Such a Fe concentration fluctuation was reported especially in heavily Fe doped samples [24,25]. It is worth mentioning that such a strong Auger peak was also observed in the case of Fe-doped Ge [35]. In addition to the Auger peak, there are resonantly enhanced features around −1.7 and −10.3 eV, denoted by α and β, respectively. Unlike the Auger peak, these peaks do not disperse with incident photon energy, representing a local excitation of Fe 3*d* states including charge transfer from ligand orbitals accompanying the photoemission process. Such resonance features are widely observed in transition-metal oxides, where the 3*d* electrons are well localized and strongly correlated [53–56]. Those local excitation peaks were almost absent in the case of Fe-doped Ge [35], suggesting that Fe 3*d* electrons in (Ga,Fe)Sb are more correlated or more localized than those in Ge:Fe. Considering that the Fe 3*d* density of states (DOS) should not be located as deep as 10 eV below E_{F}, at least feature β can be attributed to a charge-transfer satellite. In order to highlight subtle features, the second-derivative images of the RPES spectra are shown in Figs. 3(g) and 3(h), where the dispersive normal Auger peak and resonantly enhanced peaks α and β can be seen, as described above. These features are commonly seen in both samples; however, there exists a difference, as indicated by red dashed lines in Figs. 3(g) and 3(h). For the 6% Fe sample, two features are observed around 6.8 and 3.1 eV in the entire photon energy range, while for the 13.7% Fe sample, there is

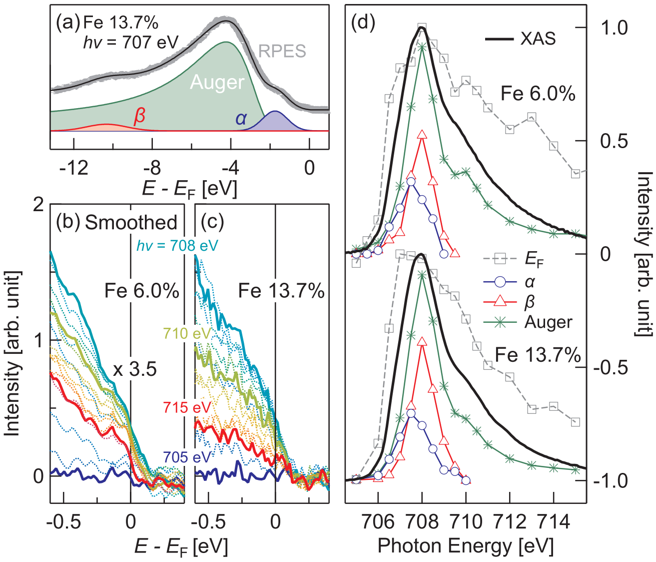

FIG. 4. (a) RPES spectrum of the 13.7% Fe-doped sample taken with $h\nu = 707$ eV (thick gray curve) and fitting results (black curve). Fitting components of two Gaussian functions for features α and β and one asymmetric Gaussian function for the Auger peak are also shown separately. (b) and (c) RPES spectra of the 6% and 13.7% Fe-doped samples near E_F. Here, the colors are the same as those used in Figs. 3(a) and 3(d). Note that the RPES spectra of the 6% Fe-doped sample have been smoothed and multiplied by 3.5 for easy comparison. (d) Constant-initial-state spectra for features α and β and the intensity at E_F and the Auger peak intensity as functions of photon energy. For comparison, XAS spectra are also plotted.

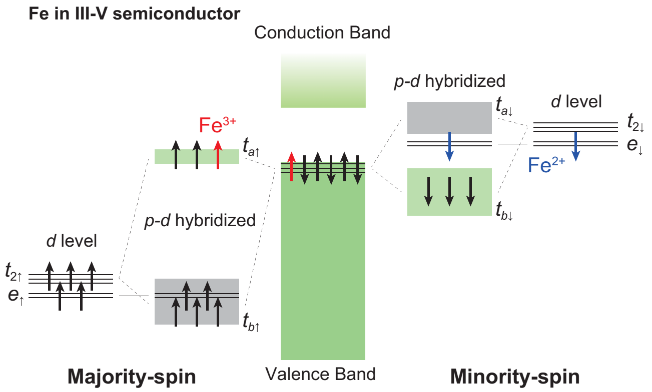

FIG. 5. Schematic energy diagram of Fe-doped III-V semiconductors. The d levels of Fe are shown on the sides, and the valence band and the conduction band of the host GaSb are shown by green boxes in the middle. Due to p-$d(t_2)$ hybridization, the t_2 orbitals are split into the bonding (t_b) and antibonding (t_a) states having both p and t_2 characters. States with predominant p and t_2 characters are indicated by green and gray boxes, respectively. The electron occupancy of the Fe^{3+} state is illustrated by red and black arrows, while that of Fe^{2+} is illustrated by blue and black arrows.

only one feature around 4 eV. This may imply the difference in the electronic structure between the two samples. Probably, the $3d$ states are more localized or more correlated in the 6% Fe-doped sample because the distance between adjacent Fe atoms is longer and the Fe $3d$ bandwidth would be narrower than in the 13.7% Fe-doped sample.

For the purpose of examining the nature of resonance enhancement, it is useful to plot the intensity at a fixed binding energy as a function of incident photon energy, namely, a constant-initial-state (CIS) spectrum. In order to eliminate the effect of the overlapping Auger peak from the CIS spectra and to extract the resonance behavior of features α and β, we have employed curve fitting as shown in Fig. 4(a). In Fig. 4(a), resonance peaks α and β are fitted by Gaussian functions, and the Auger peak, with its tail, is fitted by the asymmetric Gaussian function introduced in Ref. [57]. CIS spectra for features α and β were obtained from the peak areas of the Gaussian functions. This is an *ad hoc* procedure, but still, it provides a reasonable description of the resonance enhancement.

Figures 4(b) and 4(c) show the RPES spectra on an expanded scale near E_F. The data for the 6% Fe-doped sample have been smoothed and multiplied by 3.5 for ease of comparison with the data for the 13.7% Fe-doped sample. As can be seen, the spectral intensities at E_F for both samples are enhanced on resonance, suggesting that Fe $3d$ states make a finite contribution to the DOS at E_F. Here, the CIS spectrum at E_F is defined as the area of RPES spectra between $E - E_F = -0.6$ and 0.2 eV.

Thus-obtained CIS spectra for features α, β and the intensity at E_F are plotted in Fig. 4(d) together with the Auger peak height as a function of photon energy and the XAS spectra. The CIS spectrum for feature α is peaked at $h\nu = 707.5$ eV, but that for feature β is peaked at a higher photon energy of $h\nu = 708$ eV for both samples. The difference in the CIS peak positions implies that the broad XAS spectra actually consist of different kinds of excitations, which may correspond to peaks c and d in the inset of Fig. 2, probably involving different types of $3d$ orbitals, i.e., t_2 and e orbitals, rather than excitation into a single kind of broad metallic bands as in the case of a bcc Fe metal. We note that the CIS spectra of features α and β vanish around a photon energy of 710 eV, at which the extrinsic Fe^{3+} shoulder exists on each XAS spectrum. Therefore, the observed resonance features are not from surface oxides but are most likely intrinsic.

IV. DISCUSSION

Figure 5 illustrates the basic electronic structure of substitutional Fe in GaSb. The valence and conduction bands of GaSb are shown in the middle by large green boxes, and the Fe $3d$ levels are shown on both the right-hand and left-hand sides. Each arrow represents an electron with a specific spin. At the substitutional sites, the Fe $3d$ level is split into the doubly degenerate lower e level and the triply degenerate higher t_2 level due to the crystal field of T_d symmetry. Due to the strong p-$d(t_2)$ hybridization, the Fe t_2 orbitals and the ligand Sb p orbitals form bonding (t_b) and antibonding (t_a) states with mixed t_2 and p characters. Those levels with predominant t_2 and p characters are indicated by gray and green boxes, respectively. As for the majority-spin states, where the $t_{2\uparrow}$ level is located well below the valence-band maximum because of the relatively high Sb $5p$-derived valence-band position

[58], the bonding states have predominant Fe t_2 character, and the antibonding states have predominant Sb p character. On the other hand, the minority-spin bonding states $t_{2\downarrow}$ consist primarily of Sb p orbitals, and the antibonding states consist of Fe t_2 orbitals. Possible effects of interstitial Fe atoms have not been considered because they would act as double/triple donors, which would not be consistent with the low carrier concentration of this system.

If Fe takes a valence of 3+ with five $3d$ electrons, the $t_{a\uparrow}$ level is fully occupied, and there exists no minority-spin $3d$ electrons (except for the small contribution in the $t_{b\downarrow}$ states). On the other hand, if the valence of Fe is 2+, the sixth $3d$ electron occupies the $e_\downarrow$ level, and one hole resides in the $t_{a\uparrow}$ level. The $e_\downarrow$ level would be at the Fermi level since it is doubly degenerate and half occupied. In Fig. 5, the Fe^{3+} electronic structure is represented by red and black arrows, while Fe^{2+} is represented by blue and black arrows. Note that the basic electronic structure of (Ga,Mn)As is qualitatively the same as the one described above. The main difference is that, in the case of (Ga,Mn)As, the $e_\downarrow$ level is empty, and a hole resides in the $t_{a\uparrow}$ level since Mn has one less electron than Fe.

From the XMCD measurements, it was suggested that there is a considerable $3d^6$ contribution to the ground state of Fe as in (In,Fe)As:Be [30,34] and Ge:Fe [47]. This suggests that there may exist a long-range p-d exchange interaction mediated by holes in $t_{a\uparrow}$ states as in the case of (Ga,Mn)As. Considering the coexistence of Fe^{2+} and Fe^{3+} states, the short-range double-exchange interaction within the $e_\downarrow$ orbitals would also be present. Note that the finite Fe PDOS at the Fermi level found by the RPES measurements can be attributed to either $t_{a,\uparrow}$ or $e_\downarrow$ states in this scenario. If this is the case, the double-exchange interaction would be more important than the p-d exchange interaction considering that ferromagnetism with a similar T_C is also observed in the n-type (In,Fe)As and (In,Fe)Sb, where the s-d exchange interaction is significantly weaker than the p-d exchange interaction. In real (Ga,Fe)Sb samples, it was reported that there is an Fe concentration fluctuation, especially when Fe is heavily doped [24,25]. The double-exchange interaction would be locally strong in Fe-rich regions and would stabilize the local ferromagnetic order. This may explain the observed convex line shape of the M-T curves [24], indicating the existence of superparamagnetism even above T_C and the itinerancy of Fe $3d$ electrons observed in the present XAS/XMCD and RPES measurements. The mechanism described above is very different from how ferromagnetism appears in (Ga,Mn)As. That is, in (Ga,Mn)As, Mn atoms are randomly and uniformly distributed [59], thus having sharp ferromagnetic transitions with concave M-T curves [16], and only $t_{a\uparrow}$ orbitals play a major role in stabilizing ferromagnetic order. As a result of the uniform Mn distribution, Mn $3d$ electrons are more localized, leading to the prominent multiplet features in XAS and XMCD spectra [60] and much lower RPES intensities at the Fermi level [34]. Therefore, it can be said that nonuniform distribution of Fe atoms is the key for the high T_C's of the Fe-doped III-V FMSs.

The Fe^{2+} scenario described above, however, may not explain the fact that the carrier concentration of (Ga,Fe)Sb obtained by Hall measurements is not more than $\sim 10^{19}$ cm^{-3} [24], two orders of magnitude smaller than doped Fe atoms. One possible explanation is that the carriers are strongly trapped inside the Fe-rich regions and macroscopic carrier transport occurs via hopping between those Fe-rich regions. Such a model was introduced by Kaminski and Das Sarma [61] and was applied to Ge:Mn [62], Ge:Fe [63], and (Zn,Cr)Te [64] to describe their insulating/semiconducting natures and low carrier concentrations ($\sim 10^{18}$ cm^{-3} for Ge:Mn [62] and Ge:Fe [65], $\sim 10^{15}$ cm^{-3} for (Zn,Cr)Te [66]). Note that, although the low carrier concentration of (Ga,Fe)Sb would be explained by the Fe^{3+} scenario instead, where only the p-d exchange interaction is present, it seems difficult to explain why ferromagnetism is universally observed in the other Fe-doped FMSs regardless of the carrier type. It is worth mentioning that a recent theoretical calculation [67] pointed out the important role of superexchange interaction. In order to resolve the puzzle and to fully understand the peculiar nature of the ferromagnetism in the Fe-doped FMSs, further theoretical and experimental studies are necessary.

V. SUMMARY

In the present work, we have studied the electronic structure and the magnetism of the p-type ferromagnetic semiconductor (Ga,Fe)Sb, whose Curie temperature exceeds room temperature, using XAS, XMCD, and RPES. The line shapes of XAS and XMCD spectra suggested that the ferromagnetism is of intrinsic origin. XMCD sum rules yielded an unquenched large orbital moment, implying the considerable $3d^6$ contribution to the ground state of Fe. The valence-band RPES spectra showed a dispersive Auger peak and nondispersive resonantly enhanced peaks, which are fingerprints of the itinerant and correlated nature of the Fe $3d$ electrons, respectively. It was also found that there is a finite Fe PDOS at the Fermi level. This has been attributed to a majority-spin antibonding p-$d(t_2)$ hybridized state and/or minority-spin e state, both of which can play a role in stabilizing the ferromagnetic order through p-d exchange interaction and double-exchange interaction, respectively.

ACKNOWLEDGMENTS

This work was supported by Grants-in-Aid for Scientific Research from the JSPS (Grants No. 15H02109, No. 15K17696, No.16H02095, and No. 17H04922) and CREST of JST (Grant No. JPMJCR1777). The experiment was done under the Shared Use Program of JAEA Facilities (Proposals No. 2015B-E24 and No. 2016A-E27) with the approval of the Nanotechnology Platform Project supported by MEXT (Proposals No. A-15-AE-0041 and No. A-16-AE-0011). The synchrotron radiation experiments were performed at the JAEA beamline BL23SU in SPring-8 (Proposals No. 2015B3881 and No. 2016A3831). S.S., L.D.A., Y.K.W., and M.H. acknowledge support from the Program for Leading Graduate Schools; L.D.A., Y.K.W., and M.H. acknowledge support from the JSPS Fellowship for Young Scientists. P.N.H. acknowledges support from the Yazaki Memorial Foundation for Science and Technology, the Murata Science Foundation, and the Toray Science Foundation. A.F. acknowledges support as an adjunct member of the Center for Spintronics Research Network (CSRN), the University of Tokyo, under the Spintronics Research Network of Japan (Spin-RNJ).

[1] S. A. Wolf, D. D. Awschalom, R. A. Buhrman, J. M. Daughton, S. von Molnár, M. L. Roukes, A. Y. Chtchelkanova, and D. M. Treger, Science **294**, 1488 (2001).

[2] I. Žutić, J. Fabian, and S. Das Sarma, Rev. Mod. Phys. **76**, 323 (2004).

[3] D. D. Awschalom and M. E. Flatte, Nat. Phys. **3**, 153 (2007).

[4] J. K. Furdyna, J. Appl. Phys. **64**, R29 (1988).

[5] T. Jungwirth, J. Sinova, J. Mašek, J. Kučera, and A. H. MacDonald, Rev. Mod. Phys. **78**, 809 (2006).

[6] K. Sato, L. Bergqvist, J. Kudrnovský, P. H. Dederichs, O. Eriksson, I. Turek, B. Sanyal, G. Bouzerar, H. Katayama-Yoshida, V. A. Dinh, T. Fukushima, H. Kizaki, and R. Zeller, Rev. Mod. Phys. **82**, 1633 (2010).

[7] T. Dietl and H. Ohno, Rev. Mod. Phys. **86**, 187 (2014).

[8] T. Jungwirth, J. Wunderlich, V. Novák, K. Olejník, B. L. Gallagher, R. P. Campion, K. W. Edmonds, A. W. Rushforth, A. J. Ferguson, and P. Němec, Rev. Mod. Phys. **86**, 855 (2014).

[9] M. Tanaka, S. Ohya, and P. N. Hai, Appl. Phys. Rev. **1**, 011102 (2014).

[10] H. Munekata, H. Ohno, S. von Molnar, A. Segmüller, L. L. Chang, and L. Esaki, Phys. Rev. Lett. **63**, 1849 (1989).

[11] H. Ohno, H. Munekata, T. Penney, S. von Molnár, and L. L. Chang, Phys. Rev. Lett. **68**, 2664 (1992).

[12] H. Ohno, A. Shen, F. Matsukura, A. Oiwa, A. Endo, S. Katsumoto, and Y. Iye, Appl. Phys. Lett. **69**, 363 (1996).

[13] T. Hayashi, M. Tanaka, T. Nishinaga, H. Shimada, H. Tsuchiya, and Y. Otuka, J. Cryst. Growth **175–176**, 1063 (1997).

[14] A. Van Esch, L. Van Bockstal, J. De Boeck, G. Verbanck, A. S. van Steenbergen, P. J. Wellmann, B. Grietens, R. Bogaerts, F. Herlach, and G. Borghs, Phys. Rev. B **56**, 13103 (1997).

[15] H. Ohno, D. Chiba, F. Matsukura, T. Omiya, E. Abe, T. Dietl, Y. Ohno, and K. Ohtani, Nature (London) **408**, 944 (2000).

[16] M. Sawicki, D. Chiba, A. Korbecka, Y. Nishitani, J. A. Majewski, F. Matsukura, T. Dietl, and H. Ohno, Nat. Phys. **6**, 22 (2010).

[17] S. Koshihara, A. Oiwa, M. Hirasawa, S. Katsumoto, Y. Iye, C. Urano, H. Takagi, and H. Munekata, Phys. Rev. Lett. **78**, 4617 (1997).

[18] T. Schallenberg and H. Munekata, Appl. Phys. Lett. **89**, 042507 (2006).

[19] L. Chen, X. Yang, F. Yang, J. Zhao, J. Misuraca, P. Xiong, and S. von Molnár, Nano Lett. **11**, 2584 (2011).

[20] P. N. Hai, D. Sasaki, L. D. Anh, and M. Tanaka, Appl. Phys. Lett. **100**, 262409 (2012).

[21] P. N. Hai, L. D. Anh, and M. Tanaka, Appl. Phys. Lett. **101**, 252410 (2012).

[22] P. N. Hai, L. D. Anh, S. Mohan, T. Tamegai, M. Kodzuka, T. Ohkubo, K. Hono, and M. Tanaka, Appl. Phys. Lett. **101**, 182403 (2012).

[23] N. T. Tu, P. N. Hai, L. D. Anh, and M. Tanaka, Appl. Phys. Lett. **105**, 132402 (2014).

[24] N. T. Tu, P. N. Hai, L. D. Anh, and M. Tanaka, Phys. Rev. B **92**, 144403 (2015).

[25] N. T. Tu, P. N. Hai, L. D. Anh, and M. Tanaka, Appl. Phys. Lett. **108**, 192401 (2016).

[26] L. D. Anh, D. Kaneko, P. N. Hai, and M. Tanaka, Appl. Phys. Lett. **107**, 232405 (2015).

[27] N. T. Tu, P. N. Hai, L. D. Anh, and M. Tanaka, Appl. Phys. Express **11**, 063005 (2018).

[28] N. T. Tu, P. N. Hai, L. D. Anh, and M. Tanaka, Appl. Phys. Lett. **112**, 122409 (2018).

[29] A. V. Kudrin, Y. A. Danilov, V. P. Lesnikov, M. V. Dorokhin, O. V. Vikhrova, D. A. Pavlov, Y. V. Usov, I. N. Antonov, R. N. Kriukov, A. V. Alaferdov, and N. A. Sobolev, J. Appl. Phys. **122**, 183901 (2017).

[30] S. Sakamoto, L. D. Anh, P. N. Hai, G. Shibata, Y. Takeda, M. Kobayashi, Y. Takahashi, T. Koide, M. Tanaka, and A. Fujimori, Phys. Rev. B **93**, 035203 (2016).

[31] P. Carra, B. T. Thole, M. Altarelli, and X. Wang, Phys. Rev. Lett. **70**, 694 (1993).

[32] B. T. Thole, P. Carra, F. Sette, and G. van der Laan, Phys. Rev. Lett. **68**, 1943 (1992).

[33] O. Rader, C. Pampuch, A. M. Shikin, W. Gudat, J. Okabayashi, T. Mizokawa, A. Fujimori, T. Hayashi, M. Tanaka, A. Tanaka, and A. Kimura, Phys. Rev. B **69**, 075202 (2004).

[34] M. Kobayashi, I. Muneta, Y. Takeda, Y. Harada, A. Fujimori, J. Krempaský, T. Schmitt, S. Ohya, M. Tanaka, M. Oshima, and V. N. Strocov, Phys. Rev. B **89**, 205204 (2014).

[35] S. Sakamoto, Y. K. Wakabayashi, Y. Takeda, S.-i. Fujimori, H. Suzuki, Y. Ban, H. Yamagami, M. Tanaka, S. Ohya, and A. Fujimori, Phys. Rev. B **95**, 075203 (2017).

[36] H. Suzuki, K. Zhao, G. Shibata, Y. Takahashi, S. Sakamoto, K. Yoshimatsu, B. J. Chen, H. Kumigashira, F.-H. Chang, H.-J. Lin, D. J. Huang, C. T. Chen, B. Gu, S. Maekawa, Y. J. Uemura, C. Q. Jin, and A. Fujimori, Phys. Rev. B **91**, 140401(R) (2015).

[37] H. Suzuki, G. Q. Zhao, K. Zhao, B. J. Chen, M. Horio, K. Koshiishi, J. Xu, M. Kobayashi, M. Minohara, E. Sakai, K. Horiba, H. Kumigashira, B. Gu, S. Maekawa, Y. J. Uemura, C. Q. Jin, and A. Fujimori, Phys. Rev. B **92**, 235120 (2015).

[38] K. W. Edmonds, N. R. S. Farley, R. P. Campion, C. T. Foxon, B. L. Gallagher, T. K. Johal, G. van der Laan, M. MacKenzie, J. N. Chapman, and E. Arenholz, Appl. Phys. Lett. **84**, 4065 (2004).

[39] C. T. Chen, Y. U. Idzerda, H.-J. Lin, N. V. Smith, G. Meigs, E. Chaban, G. H. Ho, E. Pellegrin, and F. Sette, Phys. Rev. Lett. **75**, 152 (1995).

[40] V. K. Verma, V. R. Singh, K. Ishigami, G. Shibata, T. Harano, T. Kadono, A. Fujimori, T. Koide, K. Ohgushi, and Y. Tokura, Photon Fact. Act. Rep. 2011 **29**, 129 (2012).

[41] S. Brice-Profeta, M.-A. Arrio, E. Tronc, N. Menguy, I. Letard, C. C. dit Moulin, M. Noguès, C. Chanéac, J.-P. Jolivet, and P. Sainctavit, J. Magn. Magn. Mater. **288**, 354 (2005).

[42] D. Wu, D. J. Keavney, R. Wu, E. Johnston-Halperin, D. D. Awschalom, and J. Shi, Phys. Rev. B **71**, 153310 (2005).

[43] J. Stöhr and H. König, Phys. Rev. Lett. **75**, 3748 (1995).

[44] X. Lin, C. Niu, F. Pan, H. Chen, and X. Wang, Phys. B (Amsterdam, Neth.) **521**, 371 (2017).

[45] Y. Teramura, A. Tanaka, and T. Jo, J. Phys. Soc. Jpn. **65**, 1053 (1996).

[46] C. Piamonteze, P. Miedema, and F. M. F. de Groot, Phys. Rev. B **80**, 184410 (2009).

[47] Y. K. Wakabayashi, S. Sakamoto, Y.-h. Takeda, K. Ishigami, Y. Takahashi, Y. Saitoh, H. Yamagami, A. Fujimori, M. Tanaka, and S. Ohya, Sci. Rep. **6**, 23295 (2016).

[48] J. Stöhr, J. Magn. Magn. Mater. **200**, 470 (1999).

[49] K. W. Edmonds, C. Binns, S. H. Baker, S. C. Thornton, C. Norris, J. B. Goedkoop, M. Finazzi, and N. B. Brookes, Phys. Rev. B **60**, 472 (1999).

[50] If the total moment of $4.0\mu_\mathrm{B}$ is assumed, the induced magnetic moment of the paramagnetic sample would become $1.0\mu_\mathrm{B}$ at $T = 5$ K and $\mu_0 H = 1$ T following the Brillouin function.

[51] S. Hüfner, S.-H. Yang, B. S. Mun, C. S. Fadley, J. Schäfer, E. Rotenberg, and S. D. Kevan, Phys. Rev. B **61**, 12582 (2000).

[52] G. Levy, R. Sutarto, D. Chevrier, T. Regier, R. Blyth, J. Geck, S. Wurmehl, L. Harnagea, H. Wadati, T. Mizokawa, I. S. Elfimov, A. Damascelli, and G. A. Sawatzky, Phys. Rev. Lett. **109**, 077001 (2012).

[53] A. Fujimori, M. Saeki, N. Kimizuka, M. Taniguchi, and S. Suga, Phys. Rev. B **34**, 7318 (1986).

[54] A. Fujimori, N. Kimizuka, M. Taniguchi, and S. Suga, Phys. Rev. B **36**, 6691 (1987).

[55] R. J. Lad and V. E. Henrich, Phys. Rev. B **39**, 13478 (1989).

[56] J.-S. Kang, J. H. Kim, A. Sekiyama, S. Kasai, S. Suga, S. W. Han, K. H. Kim, T. Muro, Y. Saitoh, C. Hwang, C. G. Olson, B. J. Park, B. W. Lee, J. H. Shim, J. H. Park, and B. I. Min, Phys. Rev. B **66**, 113105 (2002).

[57] M. Schmid, H.-P. Steinrück, and J. M. Gottfried, Surf. Interface Anal. **46**, 505 (2014).

[58] I. Vurgaftman, J. R. Meyer, and L. R. Ram-Mohan, J. Appl. Phys. **89**, 5815 (2001).

[59] M. Kodzuka, T. Ohkubo, K. Hono, F. Matsukura, and H. Ohno, Ultramicroscopy **109**, 644 (2009).

[60] Y. Takeda, M. Kobayashi, T. Okane, T. Ohkochi, J. Okamoto, Y. Saitoh, K. Kobayashi, H. Yamagami, A. Fujimori, A. Tanaka, J. Okabayashi, M. Oshima, S. Ohya, P. N. Hai, and M. Tanaka, Phys. Rev. Lett. **100**, 247202 (2008).

[61] A. Kaminski and S. Das Sarma, Phys. Rev. B **68**, 235210 (2003).

[62] N. Pinto, L. Morresi, M. Ficcadenti, R. Murri, F. D'Orazio, F. Lucari, L. Boarino, and G. Amato, Phys. Rev. B **72**, 165203 (2005).

[63] Y. Ban, Y. K. Wakabayashi, R. Nakane, and M. Tanaka, J. Appl. Phys. **124**, 113902 (2018).

[64] M. G. Sreenivasan, K. L. Teo, X. Z. Cheng, M. B. A. Jalil, T. Liew, T. C. Chong, A. Y. Du, T. K. Chan, and T. Osipowicz, J. Appl. Phys. **102**, 053702 (2007).

[65] Y. Ban, Y. Wakabayashi, R. Akiyama, R. Nakane, and M. Tanaka, AIP Adv. **4**, 097108 (2014).

[66] H. Saito, W. Zaets, S. Yamagata, Y. Suzuki, and K. Ando, J. Appl. Phys. **91**, 8085 (2002).

[67] H. Shinya, T. Fukushima, A. Masago, K. Sato, and H. Katayama-Yoshida, J. Appl. Phys. **124**, 103902 (2018).